Supplementary Information

Average Structure and Symmetry Analysis

Mn[Co]-PBA crystals are known to adopt a cubic average structure, represented in Fig. S1. The deviations from cubic symmetry due to strain or the formation of ferroelastic domains can appear in peak splitting. High-resolution reciprocal space mapping is sensitive to such splitting. We conducted high-resolution reciprocal space mapping on 18 Bragg peaks. Three rocking curves of the measured peaks 222, 026, and 080 are displayed in Fig. S2. All the measured peaks are sharp; we observed no peak splitting for all measured peaks. The width of the rocking curves is close to the instrument resolution and to the peak width of a silicon crystal. Thus, we see no indication of a reduction in symmetry in the average structure due to strain domains.

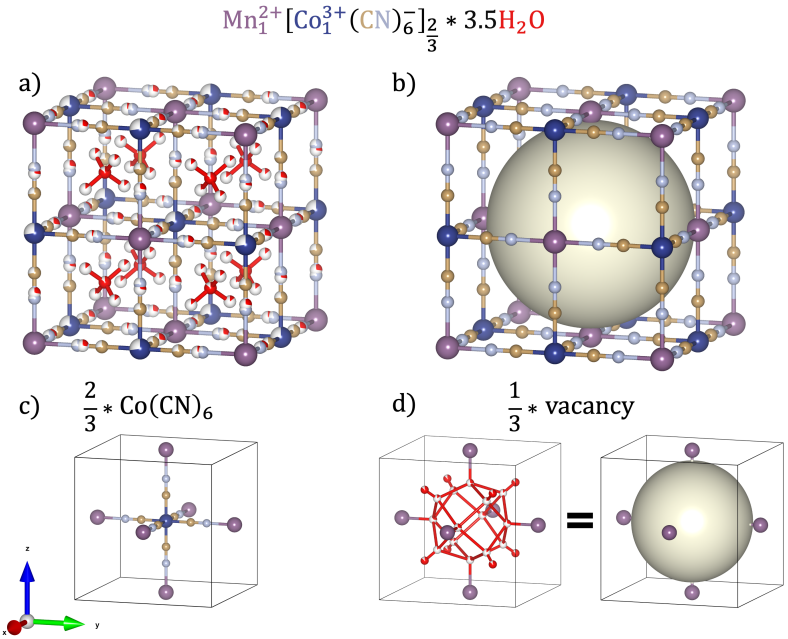


Figure S1. (a) Average structure of Mn[Co]-PBA, with space group $Fm\bar{3}m$. Mn and Co occupy alternate vertices in the FCC lattice and are connected with CN linkers (c). 1/3 of $Co(CN)_6$ positions are vacant. The vacancy, represented by a beige sphere in the simplified representation (b), in the actual structure, is filled with 14 water molecules, represented by red circles (d).

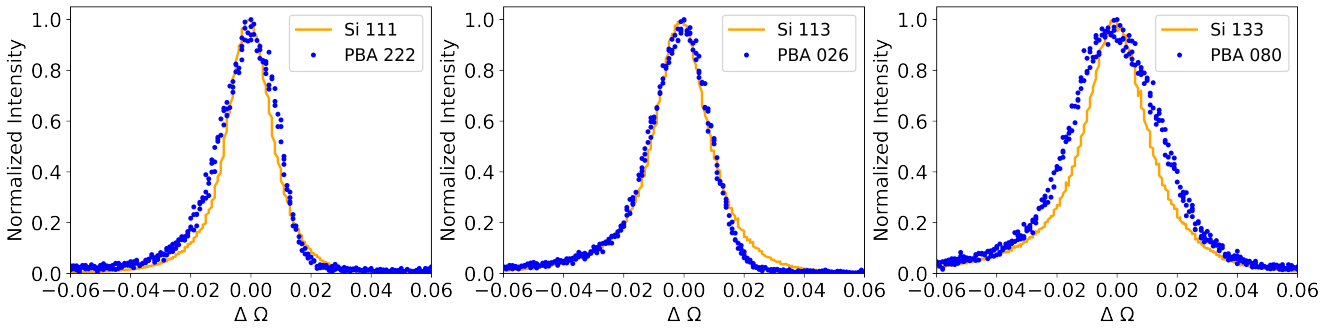


Figure S2. Results of high-resolution X-ray diffraction measurement. The panels show the rocking curves for 222, 026, and 080 reflections of Mn[Co]-PBA crystal. Rocking curves show no splitting and the FWHM width of each measured curve is below 0.02^o, comparable to the widths of rocking curves of silicon crystal at similar angles. The intensity is integrated inside the detector and represented as a function of rocking angle ($\Delta\ \Omega$).

We further analyzed the average structure in Mn[Co]-PBAs by collecting single-crystal Bragg diffraction data from an untwinned portion of the crystal. Collected Bragg peaks were integrated and scaled using the XDS software. For this, we have chosen tetragonal symmetry to ensure that the scaling procedure does not artificially increase the symmetry of the dataset. The resulting integrated peaks were left unmerged. The output file is *scaf8_unmerged.hkl*. This file was then converted by xdsconv into

res_XSCALED.hkl. The files can be found in the folder *reconstruction/xds_run0_I4mmm*.

The use of XDS software is not standard in the refinement of inorganic structures, but we have chosen it since it allowed us to perform Bragg peak integration and the reconstruction of reciprocal space using the same orientation matrix. This way, we have ensured that the orientation of the tetragonal axis is correctly aligned along **c** axis, as can be seen in Fig. S3 or in three-dimensional reconstructed data (folder *reconstruction/reconstruct*).

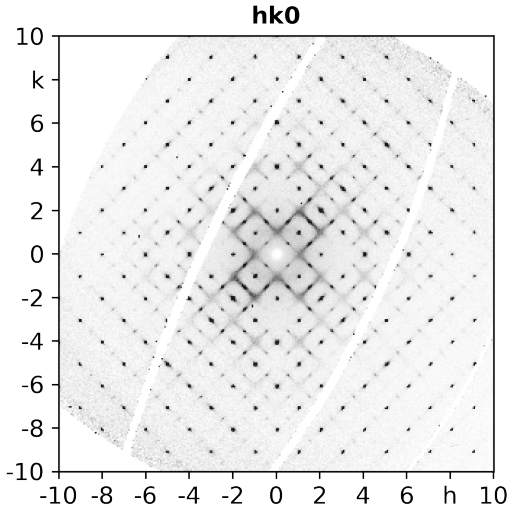


Figure S3. Reconstructed hk0 plane of 3D dataset in tetragonal setting, with 4-fold rotation aligned with 00l direction.

Next, we have used Jana2020 [43] to transform the tetragonal reflection file to the cubic setting (file *03_transformed_to_cubic.hkl*. The unit cell parameters in two given space groups, $Fm\bar{3}m$ and $I4/mmm$, are provided in Table S1.

Next, we refined tetragonal ($I4/mmm$) and cubic ($Fm\bar{3}m$) structures in ShelxL. The structure refinement in cubic symmetry resulted in the structure with parameters provided in Table S2. We have used anisotropic atomic displacement parameters for Co, Mn, C, N, and oxygen atoms, which belong to the structural water, and isotropic atomic displacement parameters for the zeolitic water.

The refinements were conducted with the following constraints:

- The occupancies of Co, C, and N atoms were set equal;
- The occupancies of structural water atoms O2 and O3 were set to 1-occ(Co);
- The atomic displacement parameters (ADP) of N and O atoms at shared positions were set equal: ADP(N1)=ADP(O2) and ADP(N2)=ADP(O3).

During refinement, we made sure that ShelxL [36] did not merge the data (option MERG 0) such that R-factors of cubic and tetragonal structures are calculated from the identical set of reflections. We also did not use the reweigthing scheme (WGHT 0) because weighting schemes use calculated intensities which are slightly different in cubic and tetragonal structure, which would mean that the weights in the two models will be different. The extinction parameter was refined but showed a relatively low value of 0.003 (tetragonal) and 0.001 (cubic). Fig. S4 displays the refined structure of Mn[Co]-PBA crystal in cubic symmetry represented in the usual cubic setting. To simplify the comparison of refined structures in two symmetries, we represent the refined cubic structure in the tetragonal setting (Fig. S5 a). The refined structure in tetragonal symmetry is represented in Fig. S5 b. The details of the refined structures in cubic and tetragonal symmetries are provided in Tables S3, and S4, respectively. The final parameters of the refinements are listed in Table S5 with F_{obs} vs F_{calc} plot for tetragonal refinement displayed in Fig. S6.

Table S1. Unit cell constants in two given spacegroups

SG	a, Å	b, Å	c, Å	α, °	β, °	γ, °
$Fm\bar{3}m$	10.411(8)	10.411(8)	10.411(8)	90	90	90
$I4/mmm$	7.362(4)	7.362(4)	10.411(8)	90	90	90

Table S2. Refined fractional coordinates x, y, z and atomic displacement parameters U_{ij} at room temperature according to cubic $Fm\bar{3}m$ spacegroup setting.

Atom	Occupancy	x	y	z	U_{11}	U_{22}	U_{33}
Co1	0.716(3)	0	0	0	0.0221(4)		
Mn1	1	0.5	0	0	0.0282(3)		
C1	0.716(3)	0.8186(4)	0	0	0.0286(16)	0.0440(13)	0.0440(13)
N1	0.716(3)	0.7030(5)	0	0	0.016(3)	0.125(3)	0.125(3)
O1	0.8599	0.75	0.75	0.75	0.181(16)		
O2	0.284(3)	0.7303(14)	0	0	0.016(3)	0.125(3)	0.125(3)
O3	0.14	0.8252(18)	0.6748(18)	0.6748(18)	0.149(11)		

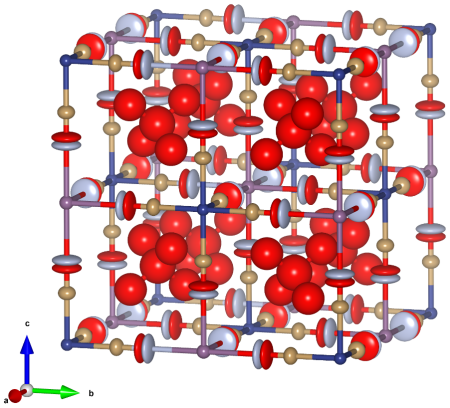


Figure S4. Result of structure refinement of Mn[Co]-PBA in cubic $Fm\bar{3}m$ space group.

Table S3. Final refinement of fractional coordinates x, y, z and atomic displacement parameters U_{ij} in cubic $Fm\bar{3}m$ spacegroup, represented in tetragonal setting.

Atom	Occupancy	x	y	z	U_{11}, U_{22}	U_{12}	U_{33}
Co1	0.716(3)	0	0	0	0.02210(7)		
Mn1	1	0.5	0.5	0	0.02820(7)		
C1	0.716(3)	0.8186(2)	0.1814(2)	0	0.0363(6)	0.0389(3)	0.0440(6)
C2	0.716(3)	0.5	0.5	0.3186(2)	0.0440(4)	0.0389(4)	0.0286(10)
N1	0.716(3)	0.7030(3)	0.297(3)	0	0.0705(11)	0.0887(7)	0.1250(16)
N2	0.716(3)	0.5	0.5	0.2030(3)	0.1250(11)	0.0887(7)	0.0160(15)
O1	0.8599	0	0.5	0.25	0.181(5)		
O2	0.284(3)	0.7303(9)	0.2697(9)	0	0.0705(11)	0.0887(7)	0.1250(16)
O3	0.284(3)	0.5	0.5	0.2303(9)	0.1250(11)	0.0887(7)	0.0160(15)
O4	0.14	0.150(2)	0.5	0.3252(16)	0.149(7)		

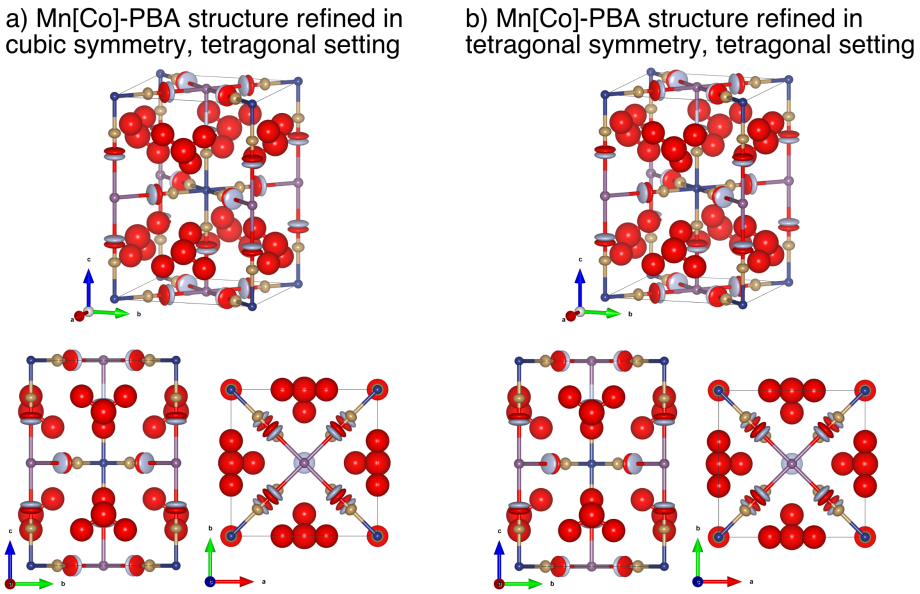


Figure S5. The resulting refined structures in (a) cubic $Fm\bar{3}m$ and (b) tetragonal $I4/mmm$ symmetry compared in the tetragonal setting.

Table S4. Final refinement of fractional coordinates x, y, z and atomic displacement parameters U_{ij} at room temperature according to $I4/mmm$ spacegroup setting.

Atom	Occupancy	x	y	z	U_{11}, U_{22}	U_{12}	U_{33}
Co1	0.716(2)	0	0	0	0.0224(3)	0.0221(2)	0.0214(3)
Mn1	1	0.5	0.5	0	0.0284(2)	0.0282(2)	0.0279(3)
C1	0.716(2)	0.8186(3)	0.1814(3)	0	0.0370(9)	0.0391(6)	0.0432(16)
C2	0.716(2)	0.5	0.5	0.3186(5)	0.0438(14)	0.0385(9)	0.0278(17)
N1	0.716(2)	0.7030(4)	0.297(4)	0	0.0705(19)	0.0881(16)	0.123(3)
N2	0.716(2)	0.5	0.5	0.2030(5)	0.126(3)	0.089(2)	0.016(4)
O1	0.86	0	0.5	0.25	0.181(10)		
O2	0.284(2)	0.7306(11)	0.2694(11)	0	0.0705(19)	0.0881(16)	0.123(3)
O3	0.284(2)	0.5	0.5	0.2293(18)	0.126(3)	0.089(2)	0.016(4)
O4	0.14	0.151(3)	0.5	0.325(2)	0.149(7)		

Table S5. Final parameters of refinement in cubic $Fm\bar{3}m$ and tetragonal $I4/mmm$ space-group settings.

Parameter	$Fm\bar{3}m$	$I4/mmm$
R^a_{int}, (%)	3.28	3.16
GOF^b(obs)	2.252	2.234
R1^c(obs), (%)	3.64	3.59
wR2^d(obs), (%)	12.45	12.34
GOF^b(all)	2.252	2.234
R1^c(all), (%)	3.9	3.84
wR2^d(all), (%)	12.87	12.76
Number of parameters refined, p	15	27
Number of reflections, n	8126	8126

[a] Reliability factor of measured dataset R_{int} is defined as $R_{int} = \sum|F_o^2 - F_o^2(mean)|/\sum|F_o^2|$, where F_o^2 means the experimental measured scattering intensity; F_c^2 is calculated intensity; F_o and F_c are observed and calculated structure factors, respectively;

[b] Goodness of fit $GOF = S = \{\sum[w(F_o^2 - F_c^2)^2]/(n-p)\}^{1/2}$, where n is the number of reflections; p is the total number of parameters refined; $w = 1/[\sigma^2(F_o^2) + (aP)^2 + bP]$; P is $[2F_c^2 + Max(F_o^2, 0)]/3$.

[c] Reliability factor $R1 = \sum||F_o| - |F_c||/\sum|F_o|$.

[d] Weighted residual factor $wR2 = \{\sum[w(F_o^2 - F_c^2)^2]/\sum[w(F_o^2)^2]\}^{1/2}$.

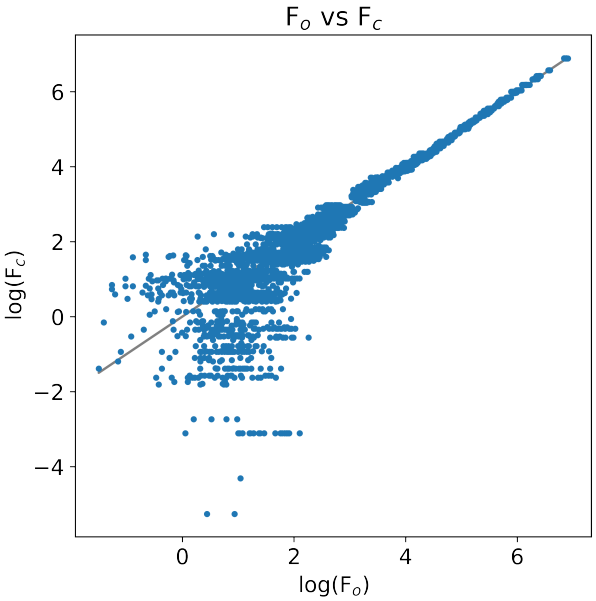


Figure S6. F_o vs F_c plot for the tetragonal structure refinement against 8126 peaks.

3D-ΔPDF Refinement

We analyze the local structure of Mn[Co]-PBA crystals using Yell software [41], which relies on 3D-ΔPDF approach [42]. 3D-ΔPDF provides information about features of the real structure that are not represented in the average structure, describing these features in terms of interatomic pair correlations. Using this method, we run the refinements of the pair correlations for building blocks separated at different lattice vectors versus the experimental diffuse scattering.

Experimentally measured diffuse scattering from Mn[Co]-PBAs consists of two parts:

- Broad diffuse scattering around Bragg peaks often referred to as “thermal-diffuse-scattering-like" (TDS-like); in this crystal, it arises mainly due to correlated static displacements in the framework (Fig. S7, green arrow).
- Crosses of diffuse scattering centered at the borders of the Brillouin zone (Fig. S7, red arrow). This diffuse scattering originates from the correlations in vacancy occupancy.

Thus, the experimental diffuse-scattering pattern can be described directly in terms of pair correlations of substitutional and displacive types. Substitutional correlation means that the occupancy of one site depends on the occupancy of the other site. It is represented by the probability of finding both sites occupied simultaneously. Displacive correlation between two sites is defined as a covariance of their translational modes.

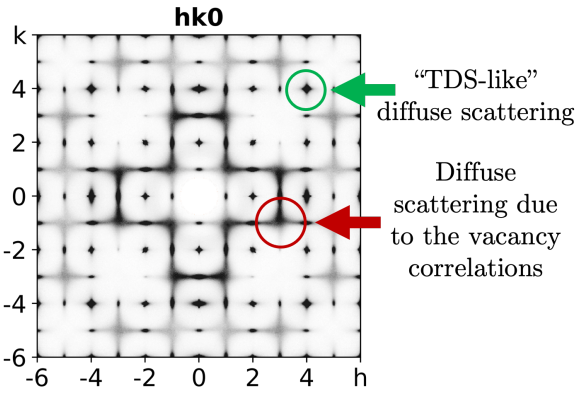


Figure S7. Reconstructed (*hk*0) plane of diffuse-scattering dataset. This dataset contains three main components: Bragg peaks at even *h*,*k*,*l*; broad diffuse scattering around Bragg peaks referred to as “thermal-diffuse-scattering-like" (green arrow); and crosses of diffuse scattering at the borders of the Brillouin zone (red arrow), which arises due to non-random $Co(CN)_6$ distribution.

The 3D-ΔPDF model of Mn[Co]-PBA is refined against the experimental three-dimensional reconstructed diffuse scattering with a rather low resolution, 200×200×200 pixels. This low resolution is required to ensure the reasonable execution time of the program and the operating memory required. Both strongly depend on the number of pixels in the experimental diffuse-scattering map, the number of interatomic pairs to be refined, and the number of parameters in the refinement [41].

TDS signal is broad, it partially overlaps with the diffuse due to vacancy correlations. This creates a substantial challenge in refining the local structure model of the substitutional type of disorder. We mitigate this problem by refining two types of disorder, substitutions and displacive, simultaneously. To run the local structure refinement, we prepare the dataset by removing the Bragg peaks from the reconstructed experimental diffuse-scattering dataset, represented in Fig. 2. We remove the Bragg peaks with a punch and fill procedure using the software Meerkat [35]. The Bragg peaks in the given dataset are sharp, so we chose the punched and filled area to be a sphere of a 2-pixel radius. Next, using Yell software, we run 3D-ΔPDF refinement for two kinds of correlations, substitutions type and displacive type, for all the pairs of building blocks within a distance of 5×5×5 unit cells radius. This simultaneous refinement of two types of correlations reproduces well the experimental data, Fig. S8, and allows disentangling of the portion of the diffuse signal that arises due to non-random disorder in vacancy occupancies from the displacive disorder, Fig. S9.

The refined model contains enough parameters to refine not only the experimental diffuse scattering but also fit the artifacts created by the punch and fill procedure, Fig. S8. However, these artifacts don’t affect the substitutional correlations in a model and are only contained in the parameters of displacive correlations, which we don’t use in the further analysis of this paper. It becomes evident that the substitutional correlations are unaffected by these artifacts if we separate the refined model into two portions: one with the substitutional correlations and one with the displacive correlations alone, Fig. S9. The refined substitutional correlations reproduce the experimental crosses of diffuse scattering and capture the loss of cubic symmetry. The refined models are provided in the supplementary file.

Table S6. Result of 3D-ΔPDF refinement: Substitutional pair correlations for the neighbors, separated by the vector (x, y, z). See the supplementary file “correlation_matrix.npz" for the complete list of pair correlations.

x	y	z	refined pair probability
0.5	0.5	0	-0.189
0	0.5	0.5	-0.132
1	0	0	0.214
0	0	1	0.273
1	0.5	0.5	0.032
0.5	0.5	1	-0.041
1	1	0	0.091
1	0	1	0.108
1	1	1	0.024
1.5	0.5	0	-0.107
1.5	0	0.5	-0.072
1	1.5	0.5	-0.005
1.5	0.5	1	-0.049
1	0.5	1.5	0.010
1.5	1.5	0	-0.055
1.5	0	1.5	-0.042
2	0	0	0.104
0	0	2	0.186

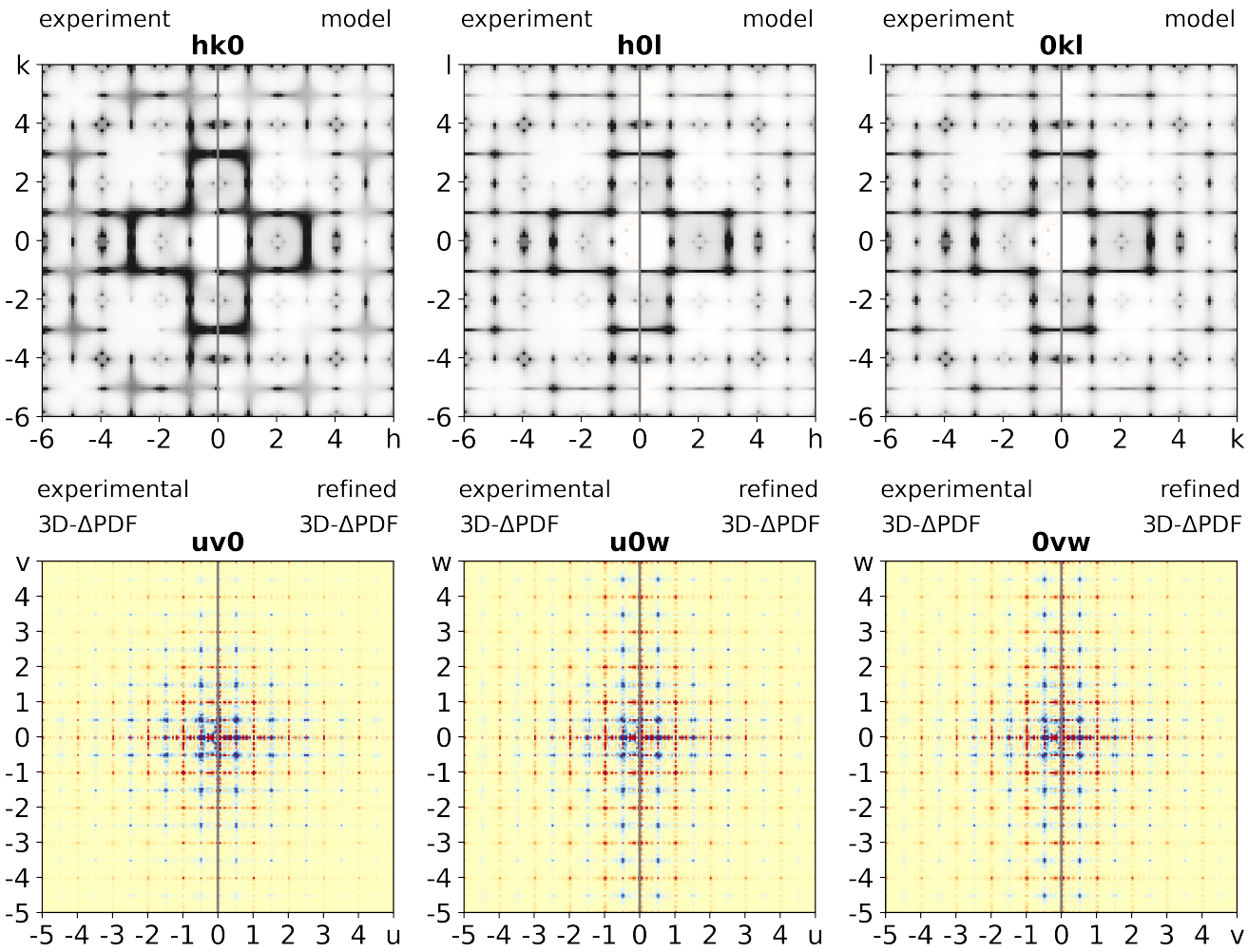


Figure S8. Comparison of the experimental data with the refined model in reciprocal (top) and 3D-ΔPDF space (bottom). The model includes substitutional and displacive pair correlations for all neighbor pairs up to the 5th unit cell.

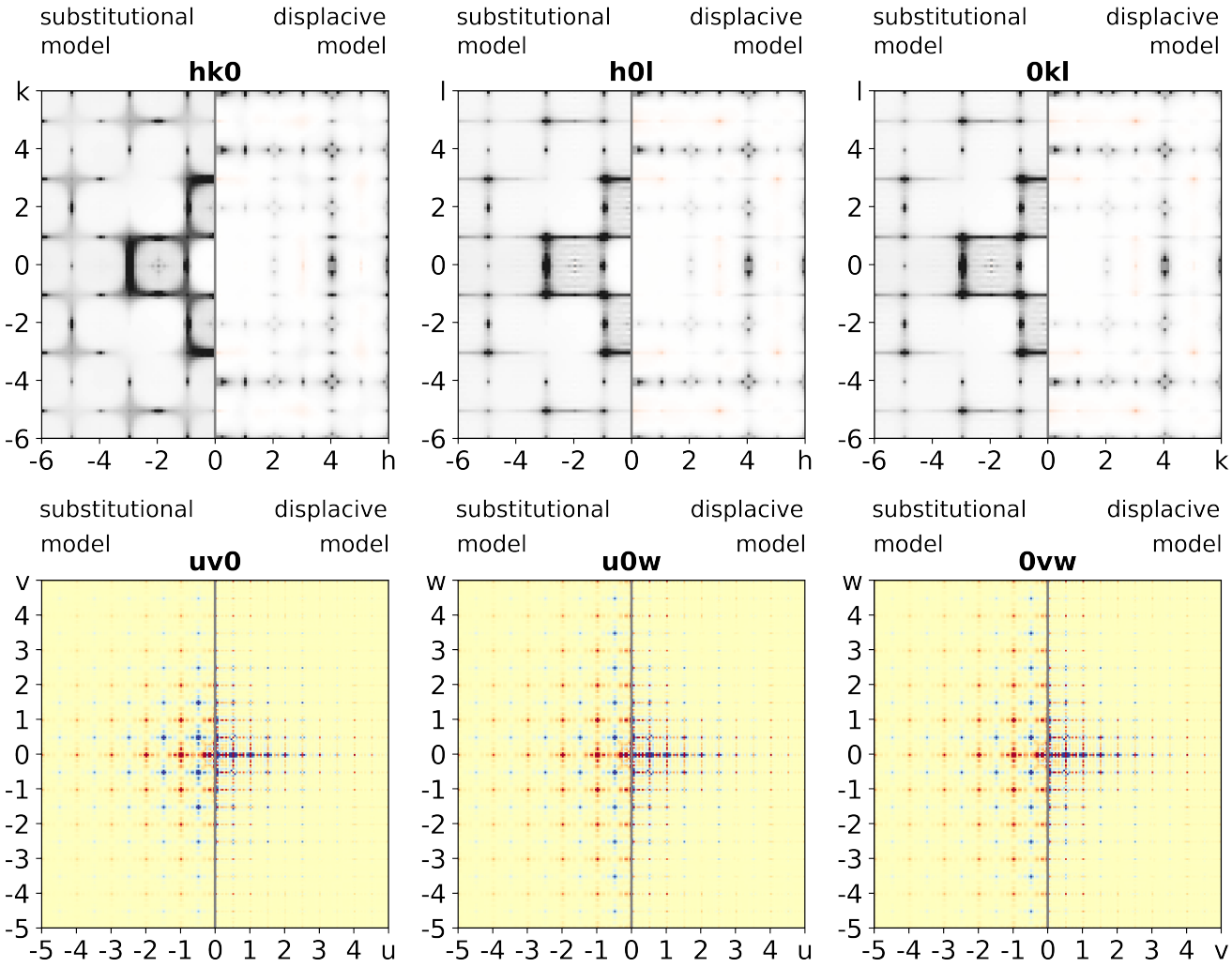


Figure S9. Models of substitutions and displacive pair correlations represented in reciprocal space (top) and 3D-ΔPDF space (bottom). The 3D-ΔPDF refinement of the experimental dataset was performed using the program Yell. Two types of correlations were refined: substitutional and displacive, for all pairs of neighbors in the model. Substitutional correlations describe the diffuse crosses at the Brillouin zone borders, while displacive correlations reproduce the diffuse scattering around Bragg peaks.

Monte Carlo Modeling

Monte Carlo simulations were carried out using custom-written code provided. Each configuration is represented by a 16x16x16 supercell. Configurations were initialized with a random distribution of vacancies, such that one-third of the sites were vacant. We represent the Monte Carlo energy of the generated structure by the Hamiltonian (Eq. 1):

$$H = \frac{1}{2}\sum_{r\in\{M\}} e_r \left[J_1 \sum_{r'\in\frac{1}{2}\langle 110\rangle} e_{r+r'} + J_{2,x,y} \sum_{r'\in\{[100],[010]\}} e_{r\pm r'} + J_{2,z} \sum_{r'\in\{[001]\}} e_{r\pm r'} \right], \tag{1}$$

where the sum is taken over all M sites at position r with the neighboring sites at $r+r'$ with states $e_{r+r'}=0$ (vacant) or $e_{r+r'}=1$ (present). The interactions in this Hamiltonian are set to:

- The nearest neighbor interaction $J_1 = 0.605$
- The second neighbors interactions $J_{2,x} = J_{2,y} = -0.0135$, and $J_{2,z} = -0.11$

For the given interaction parameters, we generate 5,000 structures. The Monte Carlo step involves a swap of one vacancy ($e_{r+r'}=0$) with one hexacyanocobaltate cluster $e_{r+r'}=1$, both chosen at random. The swap is accepted if the energy of the system is reduced; if it increases, the swap is accepted with the probability $p = \exp\left[\frac{E1-E2}{T}\right]$, where $E1$ - is the energy of the system before the swap, $E2$ - is the energy after the swap and T is Monte Carlo temperature, set to 1.3. The configurations were equilibrated for 500 epochs (one epoch corresponds to the number of steps required to visit each site twice on average) with 20 epoch steps in between each produced structure.

Fig. S10 shows the agreement of experimental diffuse scattering with diffuse scattering calculated from the structures generated by Monte Carlo. In this work, we aimed to get a reasonable agreement between the model and the experimental data, using the minimum number of interaction parameters to maintain model simplicity.

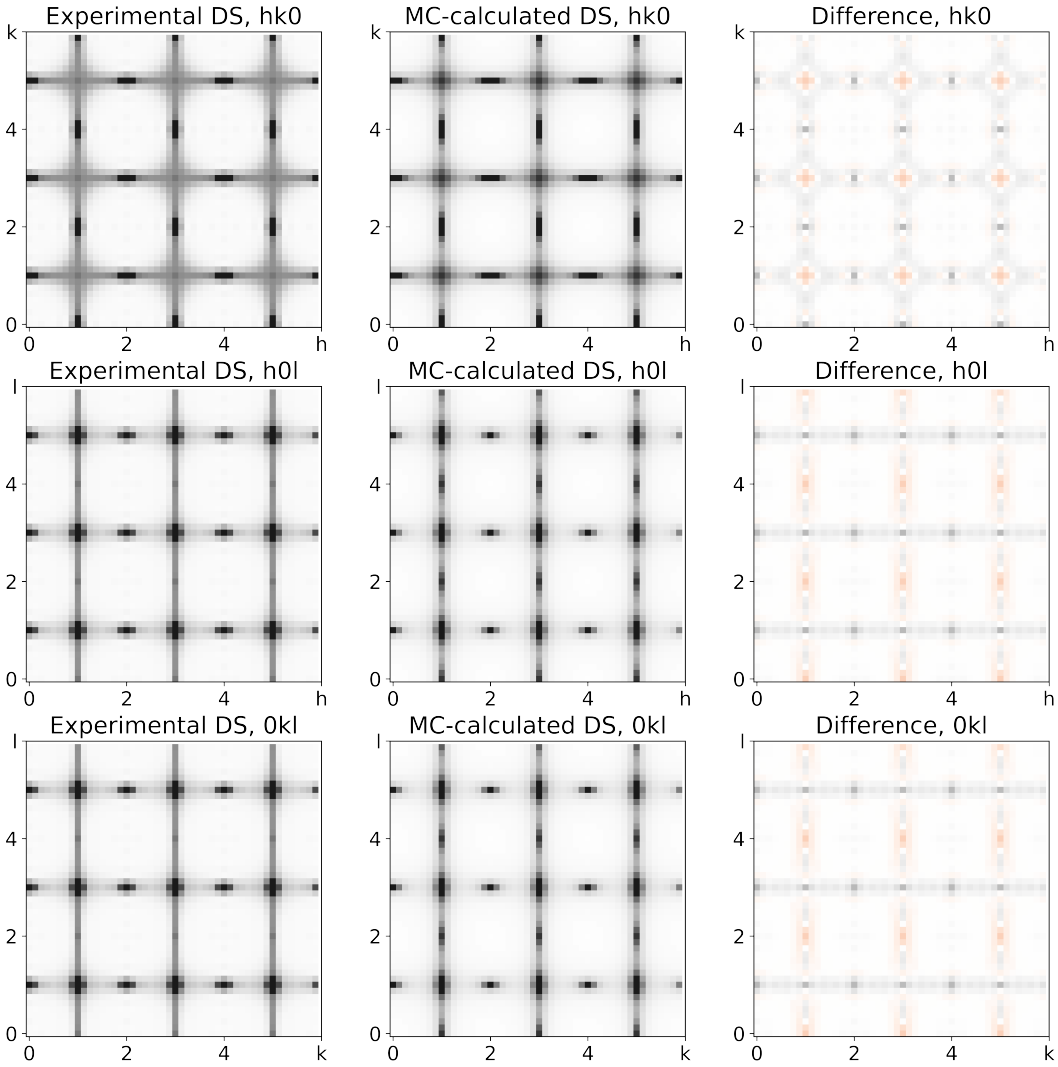


Figure S10. Comparison of the experimental diffuse scattering (Experimental DS) with diffuse scattering calculated from the structures generated by Monte Carlo (MC-calculated DS). We represent only the structure factor portion of diffuse scattering, the form-factor portion is omitted. This Monte Carlo Model relies upon interaction parameters between the nearest (J_1) and second nearest (J_2) neighbors. The first term, J_1, describes vacancy interactions between nearest neighbors along $\langle 110 \rangle$ directions, with J_1=0.605 for [110], [101], and [011] directions. The second term, J_2, describes vacancy interactions along $\langle 100 \rangle$ directions, split into $J_{2,x}$, $J_{2,y}$, and $J_{2,z}$ to reduce symmetry from cubic to tetragonal, with $J_{2,x}$=$J_{2,y}$=-0.0135 for the second nearest neighbors along [100] and [010] directions, and $J_{2,z}$=-0.11 for the second nearest neighbor along [001] direction. The Monte Carlo temperature T was set to 1.3. The R-factor for this model is 21.9 %.

Scanning electron microscopy and elemental composition

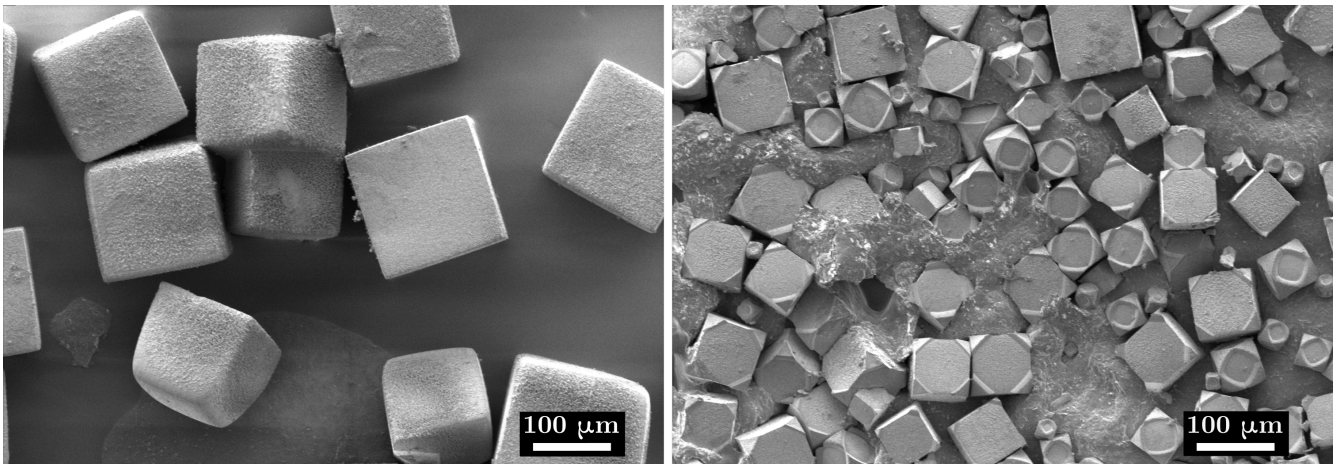


Figure S11. SEM images of the Mn[Co]-PBA crystals with distinct morphologies: cube-shaped crystals extracted from the bottom of the centrifuge tube (left) and truncated cubes extracted from the very top layer (right).

Table S7. Elemental composition of Mn[Co]-PBAs shaped as cubes determined by EDX, the value is average from three cubes.

Element	Relative atomic ratio
Mn	1
Co	0.71(2)
K	0.15(2)

Table S8. Elemental composition of Mn[Co]-PBAs shaped as truncated cubes by EDX, the value is the average from two cubes.

Element	Relative atomic ratio
Mn	1
Co	0.73(2)
K	0.16(2)

Mueller Polarimetry

The data were acquired on the setup in Fig. S12, using an exposure of 30 ms with the x20/NA 0.3 objective and 8 ms for the x4/NA 0.13 (this is subject to variation depending on the sample. See the sample descriptions for more precision). Due to the objective magnification, numerical aperture, and the sensor pixel pitch, the acquisition was performed at a resolution of 0.586 μm (respectively 1.465 μm for the x4 objective). For each field of view, we performed a polarimetric scan using the sixteen combinations of PSG [LP 0^o, EL (0.5, 0^o), RCP, LCP] and PSA [LP 0^o, EL (0.5, 0^o), RCP, LCP], recording the intensity image resulting for each [S1]. Note that EL (0.5, 0^o) stands for an elliptical state of ellipticity +0.5, aligned at 0^o, RCP is right circular polarisation, and LCP left circular polarisation. From the recorded intensity maps, we can extract the Mueller matrix of the samples at every pixel [44], and deduce from the latter their generalized birefringence properties using the Lu & Chipman polar decomposition method [45].

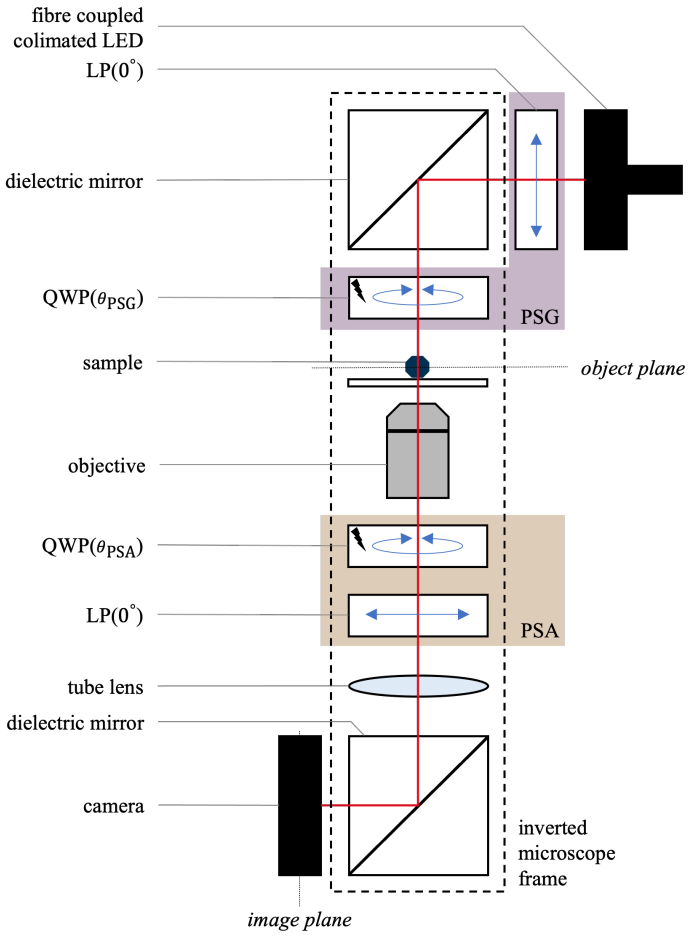


Figure S12. Setup for Mueller Polarimetry.